Identifying and controlling the order parameter for ultrafast photoinduced phase transitions in thermosalient materials

Ghasemlou, S.; Li, X.; Galimberti, D.R.; Nikitin, T.; Fausto, R.; Xu, J.; Holleman, S.; Rasing, T.; Cuppen, H.M.

DOI
10.1073/pnas.2408366121

Publication date
2024

Document Version
Final published version

Published in
Proceedings of the National Academy of Sciences of the United States of America

PNAS RESEARCH ARTICLE | CHEMISTRY

Identifying and controlling the order parameter for ultrafast photoinduced phase transitions in thermosalient materials

Saba Ghasemlou[a], Xinyue Li[a], Daria R. Galimberti[a], Timur Nikitin[b], Rui Fausto[b,c], Jialiang Xu[d], Steven Holleman[a], Theo Rasing[a], and Herma M. Cuppen[a,e,1]

Affiliations are included on p. 6.

Edited by Matteo Salvalaglio, University College London, London, United Kingdom; received May 7, 2024; accepted September 17, 2024, by Editorial Board Member Joanna Aizenberg

The drastic shape deformation that accompanies the structural phase transition in thermosalient materials offers great potential for their applications as actuators and sensors. The microscopic origin of this fascinating effect has so far remained obscure, while for technological applications, it is important to learn how to drive transitions from one phase to another. Here, we present a combined computational and experimental study, in which we have successfully identified the order parameter for the thermosalient phase transition in the molecular crystal 2,7-di([1,1'-biphenyl]-4-yl)-fluorenone. Molecular dynamics simulations reveal that the transition barrier vanishes at the transition temperature. The simulations further show that two low-frequency vibrational–librational modes are directly related to the order parameter that describes this phase transition, which is supported by experimental Raman spectroscopy studies. By applying a computational THz pulse with the proper frequency and amplitude we predict that we can photoinduce this phase transition on a picosecond timescale.

phase transitions | molecular machines | molecular dynamics | THz spectroscopy

Significance

2,7-di([1,1'-biphenyl]-4-yl)-fluorenone (4DBpFO) crystals exhibit a remarkably rapid solid-state phase transition resulting in a crystal jump. So far the underlying atomistic mechanism is poorly understood, making it an intriguing subject for study. Computationally, we have successfully identified the molecular motions driving the phase transition in 4DBpFO. The transition barrier vanishes at the transition temperature. The simulations predict that the transition can be induced by applying a pulse at the resonant frequency of the relevant motions far below the transition temperature. This brings a high level of control over the phase transition and our computational approach should be transferable to other systems to predict how to selectively trigger changes in these materials.

Mechanically responsive materials (1, 2), show a mechanical response, e.g., drastic shape change due to external stimuli, like temperature, pressure, or electromagnetic fields which make them applicable as molecular motors or switches (3–6). Most materials considered in this context are polymeric. Molecular crystals are often overlooked since they are considered brittle and their elastic properties are too hard to withstand the perpetual movements required (3). One of the advantages of crystals over amorphous material is that because of their regular structures, small perturbations in weak interactions can be amplified through the cumulative effect of the periodicity. Additionally, the periodicity of the material aids in its characterization from a structural point of view, which is crucial for the atomistic understanding of the mechanism and the design of new materials with optimal responsive properties. We do know that the origin of the mechanical response is a solid-to-solid phase transition between crystal structures of the compound, triggered by the external stimulus (4). However, much is still unknown about the underlying mechanisms of this fascinating response.

In this paper, we present a combined computational and experimental Raman study of 2,7-di([1,1′-biphenyl]-4-yl)-fluorenone crystals, or 4DBpFO, which was recently discovered as a thermosalient crystal with excellent reversibility and robustness (7) and excellent potential for THz generation (8). The thermosalient behavior of 4DBpFO is triggered by a solid-to-solid phase transition between the α and β form and is exceptional for several reasons: 1) the transition is cyclable over hundreds of cycles, 2) the transition mechanism is evidenced by a well-defined transition temperature, and low hysteresis (7), and 3) the phase transition involves a small conformational change in the molecule that leads to a packing rearrangement. The 4DBpFO crystals can be categorized as a class I thermosalient material, since it consists of molecules that are devoid of strong hydrogen-bond donors, although they do not pack in layers as most of the materials in this class (9).

While solid-to-solid phase transitions have been extensively described for simple inorganic crystals (10–12), complications arise when considering molecular crystals, where complex behaviors such as intramolecular torsions, zip-like mechanisms, and cooperativity are possible, even within unit cells (13, 14). The forces in inorganic crystals usually originate from ionic interactions. Instead, forces that lead to intramolecular rearrangement in molecular crystals are typically stronger per molecule but are much weaker between the neutrally charged organic molecules and act more locally on a

Author contributions: S.G., D.R.G., T.R., and H.M.C. designed research; S.G., X.L., D.R.G., T.N., R.F., S.H., and H.M.C. performed research; J.X. contributed new reagents/analytic tools; D.R.G., R.F., T.R., and H.M.C. supervision; and S.G., D.R.G., T.R., and H.M.C. wrote the paper.

The authors declare no competing interest.

This article is a PNAS Direct Submission. M.S. is a guest editor invited by the Editorial Board.

[1]To whom correspondence may be addressed. Email: h.cuppen@science.ru.nl.

This article contains supporting information online at https://www.pnas.org/lookup/suppl/doi:10.1073/pnas.2408366121/-/DCSupplemental.

Published November 5, 2024.

molecule-by-molecule basis (13, 15). This allows intramolecular changes in, for instance, torsional angles, to induce larger movement between molecules in both α and β phases. In this study, we focus on the α to β phase transition of 4DBpFO. By first exploring the order parameter or reaction coordinate by classical molecular dynamics (MD), we find that the barrier for transition decreases rapidly around the phase transition temperature. Second, by determining the corresponding vibrational frequencies, we identified the low-frequency (THz) vibrational–librational modes that are directly related to the order parameter that describes this phase transition. These computational results appear to be in excellent agreement with micro-Raman experiments that could be performed on both phases simultaneously. In addition, we present a computational prediction, partly supported by experiments, that the transition can be triggered in 4DBpFO by a pulse at the frequency of the lowest THz mode associated with the transition mechanism, well below the phase transition temperature.

Results

Structural Changes in the $\alpha \leftrightarrow \beta$ Phase Transition. Fig. 1*A* shows a schematic model of 4DBpFO. The molecule consists of five flat segments that can rotate with respect to each other via two pairs of dihedral angles, ϕ and θ, and their symmetry equivalent counterparts ϕ' and θ'. In both the α and the β form, the molecules are stacked in a layered-like fashion (Fig. 1). Table 1 shows the lattice parameters of both forms. Structurally both forms are very similar and only the two dihedral angles change, making the molecule more flat in the β form. This condenses the packing along the a axis and increases the distances along c (Fig. 1*B*). The overall effect is a significant change in the crystal shape—as reflected by the dashed lines in Fig. 1—which indicate the stable {101} faces. Another indication is the change in the a/c ratio (Table 1). Lattice parameters obtained by MD are added in Table 1 for comparison. These simulations are discussed in *SI Appendix*. The fact that the MD simulations closely follow the experimental results gives confidence to the applied force field (*Computational Methods*).

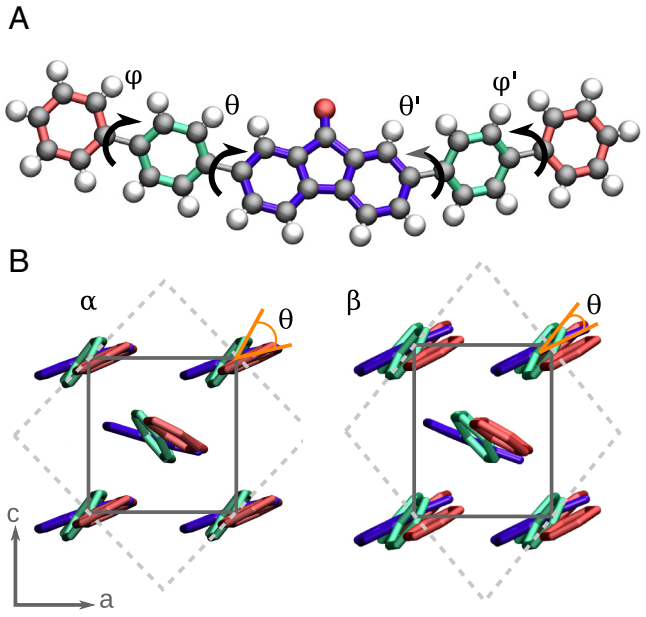

Fig. 1. (*A*) Ball-and-stick model of 4DBpFO. The colored segments can rotate with respect to each other via dihedral angles ϕ (ϕ') and θ (θ'). (*B*) Schematic representation of the consequence of the change in dihedral angles θ (in orange) for the stacking of the molecules. Solid gray lines indicate the unit cells for both forms in the (a, c) plane. The dashed gray lines represent the observed crystal shapes. The same coloring for the rotating segments is used as in (*A*).

Table 1. Structural parameters obtained through X-ray and MD simulations for the α and β forms of 4DBpFO (7)

Form		α (X-ray)	β (X-ray)	α (MD)	β (MD)
Space group		Pnma	$P2_1/n$		
Temperature (K)		443	451	400	450
Cell length (Å)	a	6.90	6.256(5)	7.07	6.39
	b	52.51	52.72(4)	52.86	53.96
	c	7.27	7.773(6)	6.91	7.58
Cell angles (°)	α	90	92.95(2)	90	95
	β	90	90	90	90
	γ	90	90	90	87
Dihedral angle θ (°)		38	22	36	18
Dihedral angle ϕ (°)		24	16	27	14
Ratio a/c		0.95	0.80	1.02	0.84

MD simulates the dynamics of the materials based on Newton's equations of motion, where the forces acting on the atoms are determined from an interaction potential, a force field in this case. The resulting dynamics is due to a combination of kinetic effects (barriers of processes) and thermodynamic effects and the full vibration of the system is considered. This is different from MC approaches such as the ones used by Ahmed et al. (16) to simulate the thermosalient transitions, which only includes macroscopic thermodynamic effects (strain interactions between cells of same or different structure) and do not include molecular details.

Previous MD simulations showed that the transition is triggered by changes in the θ and ϕ dihedral angles (7), which then lead to changes in the crystal packing. These angles can thus be used as the collective variable to describe the transition. If well-constructed, the collective variable (CV) should correspond to the order parameter or reaction coordinate of the phase transition. Here, the phase transition involves a change from space group Pnma to $P2_1/n$ 1 1, which have a group-subgroup relation. Here, we use a CV path that measures the progress of the transition by an order parameter s: at $s = 0$, the system is in the α phase, and at $s = 1$, the system is in the β phase. Fig. 2*A* plots in green the computed configurations in the (θ, ϕ) space that the system takes during the transition between the α and the β form. The red symbols indicate the two stable states. The green dots are the result of metadynamics simulations at 400 K during which the path, indicated by the purple line, is allowed to optimize. The value of s is obtained by projecting the average θ and ϕ angles on this purple line that runs from $s = 0$ (circle, α phase) to $s = 1$ (square, β phase). Here, we are particularly interested in capturing the phase transition mechanism in our metadynamics simulations and in an exploration of possible stable structures (17, 18).

Fig. 2*A* shows that the angles θ and ϕ are highly correlated. The phase transition involves mostly the rotation of the inner phenyl rings (θ) and to a lesser extent rotations of the outer rings (ϕ). Rotations of the inner rings (in green), while the outer rings (in red) stay at the same relative position with respect to the middle fluorenone segment (in blue), would correspond to equal changes in θ and ϕ, as can be seen from the schematic drawings

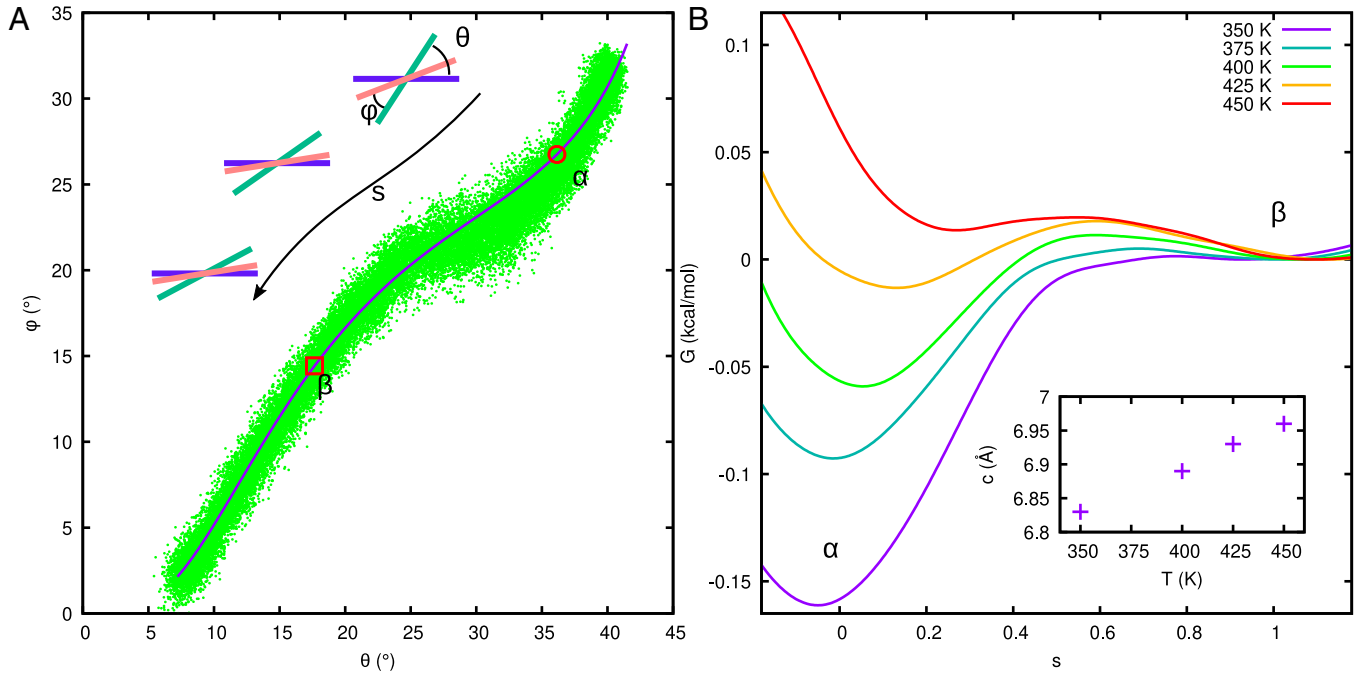

Fig. 2. (*A*) Optimized transition path as a function of θ and ϕ. The purple line represents the optimized transition path, the red symbols indicate the two stable states, the green dots indicate the configurations visited during the standard metadynamics simulation of $8 \times 1 \times 8$ unit cells at 400 K. (*B*) Free energy profile of the $\alpha \leftrightarrow \beta$ transition at different temperatures. The free energy is given per molecule in the simulation cell (256 molecules). Curves have been shifted to match $G(s = 1) = 0$. (*Inset*) Variation of *c* axis as a function of temperature for the α form.

in Fig. 2*A*. Starting from the α phase, the purple line shows that initially both the inner and outer rings rotate with respect to the fluorenone segment. Toward the end of the transition, mainly the inner rings rotate. Starting from the β phase, the mechanism is reversed, with initially mostly inner ring rotation and rotations of both rings toward the end of the transition.

Free Energy and Order Parameter of the Phase Transition. Metadynamics simulations (19–21) were performed to obtain a free energy profile along the phase transition path. Fig. 2*B* shows the result of several such metadynamics simulations for different temperatures. The profiles have been shifted to match $G(s = 1) = 0$. At 350 K, the α phase is clearly more stable than the β phase which corresponds to only a shallow minimum in the free energy. The $\alpha \rightarrow \beta$ transition is endergonic at this temperature, while there is hardly a free energy barrier for the $\beta \rightarrow \alpha$ transition. The free energy difference between the α and β phases decreases with temperature until the α free energy is roughly equal to the β free energy at 425 K, close to the experimentally observed phase transition temperature of around 450 K, although there is some crystal-to-crystal variation (7). In the simulations, β is the stable polymorphic form at 450 K and the barrier for $\alpha \rightarrow \beta$ is negligible. The change in relative stability as well as the disappearance of the transition barrier is confirmed by unbiased simulations where the α form is heated and spontaneously converts to the β form, and where the β form is cooled, leading to the $\beta \rightarrow \alpha$ transition (*SI Appendix*, Fig. S2). Notice that spontaneous transitions are observed in our relatively small simulation cells of roughly $50 \times 50 \times 50$ Å^3 without much hysteresis. This means that the critical nucleus size at the transition temperature is smaller than the simulation cell and that the critical nucleus size rapidly decreases when approaching the transition temperature. This is a signature that the surface free energy of the transition is very small, in agreement with the free energy profiles in Fig. 2*B*. This could correspond both to the phase transition picture of classical nucleation theory (22) as well as a mechanism that involves cooperative moment, since a small or zero surface free energy would mean that either the critical nucleus sizes would become small close to the transition temperature, or that many molecules could transform cooperatively without a large penalty at the interface. The simulations point more in the direction of the first scenario as shown in *SI Appendix*, Fig. S3. This is markedly different from previously studied phase transitions in molecular crystals by MD simulations, that proceed through some form of cooperative movement (23–25).

The phase transition found in the simulations proceeds much faster than the conversion speed experimentally observed for several organic materials (0.1 to 0.5 m s^{-1} = 0.01 to 0.05 Å ps^{-1}) (16). This is likely due to the limited system size and lack of defects in the simulated structure.

The Spectrum of the Order Parameter. Now that we established the order parameter *s*, the frequencies of the modes associated with the phase transition can be obtained as explained in *Computational Methods*. Fig. 3*A* shows the resulting spectra for different values of the order parameter *s*. At $s = 0$ (α phase), three different modes can be clearly distinguished, around 1.5, 4, and 5 THz. The mode around 5 THz moves to lower frequencies (right arrow in Fig. 3*A*) and then disappears upon the transition to β (increasing *s*), while the baseline appears to become more "noisy." The mode around 1.5 THz moves to lower frequencies, while at the same time the mode strongly broadens, as shown by the horizontal arrows. The mode around 4 THz moves to higher frequencies (left vertical arrow). The different modes can be assigned by obtaining similar spectra for θ and ϕ separately, since *s* is a combination of both angles. Fig. 3 *C* and *D* show the θ and ϕ spectra, respectively, clearly demonstrating that their

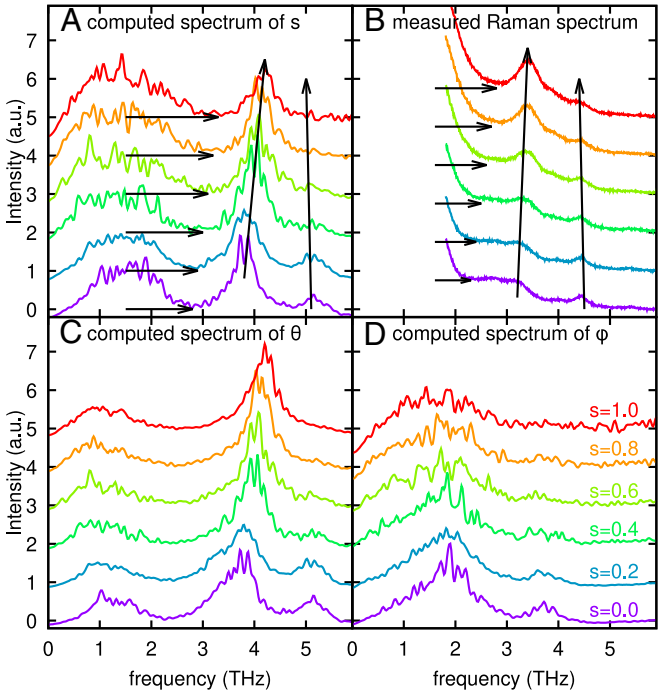

Fig. 3. Vibrational spectra of the (*A*) transition order parameter for different stages along the transition pathway *s*. Panel (*B*) gives Raman spectra taken along the phase boundary of the crystal. Calculated vibrational spectra of the (*C*) dihedral θ and (*D*) dihedral ϕ are presented in panels (*C*) and (*D*), respectively. The spectral changes, such as peak shifts and broadening, are indicated with the vertical and horizontal arrows, respectively. The increasing noise level in the baseline with increasing *s* for (*A*) and (*D*) is due to the increasing mobility of the outer rings.

combination results in the spectrum of Fig. 3*A*. These spectra also show that the disappearing mode at 5 THz is mainly due to θ. The increasing fluctuations in the baseline are due to ϕ and appear intrinsic to the β structure and are not due to a lack of statistics, since this would have resulted in a similar baseline in the θ spectrum. This is likely due to the large range of rotations of the outer rings in the β form.

The modes around 1.5 and 4 THz are clearly related to fluctuations in both θ and ϕ, although the ϕ contribution diminishes for the 4 THz mode toward the β phase. Movies S1, S3, and S4 show the mobility associated with 1.5 THz, 4 THz (θ), and 4 THz (ϕ). Higher-resolution versions can be found through https://doi.org/10.34973/j5ax-am79. The 1.5 THz mode appears to be most directly associated with the phase transition for two reasons: this mode has strong contributions of both θ and ϕ, and it is the only mode that clearly shifts toward lower frequencies during the $\alpha \rightarrow \beta$ transition. The shape of the wells in the free energy profiles in Fig. 2*B* indeed suggests that the frequency associated with the β form is lower than that of the α form because of its wider well.

To experimentally investigate the changes in the low-frequency crystal lattice vibrations, in situ micro-Raman spectra were measured from a 4DBpFO crystal at constant temperature but with a transition boundary between the α and β phase, as explained in *Materials and Methods*. The spectra were measured by scanning the excitation laser across this transition boundary and hence capture both the α and β forms for $s = 0$ and $s = 1$, respectively, as well as several stages in between. Fig. 3*B* shows the experimental Raman spectra as a function of *s*. The experimental spectra show a mode at low frequencies (<2 THz). Unfortunately, due to experimental limitations, the softening of the mode, as was evident in the simulated spectra in Fig. 3*A*, could not be observed experimentally, but the qualitative agreement between the observed broadening near 2 to 3 THz is clear (vertical arrows). This is likely due to an increase in fluctuations of the dihedral angles in β. The 4 and 5 THz modes are also observed, albeit at slightly lower frequencies (at 3.2 and 4.5 THz, respectively) than predicted computationally. The peak shift for the 4 THz feature and the disappearance of the 5 THz upon transition, however, is seen in both experimental and computational spectra. Note that the modes in the calculated *s* spectrum (Fig. 3*A*) can be Raman or IR active, and hence they do not necessarily need to appear in the experimental Raman spectra whereas also the relative intensities can be different. Furthermore, the calculated vibrational spectra only include the modes that are connected to the order parameter of the transition. This is different from the more common computational studies that aim at reproducing experimental spectra (26–28). The advantage of our approach is that we can directly "weed-out" the relevant modes from the spectrum without first assigning all features to obtain the modes relevant for the phase transition (29–31) which can be hard for very anharmonic systems.

Ultrafast Photoinduced Phase Transition. Photoinduced phase transitions allow ultrafast nonequilibrium phenomena such as THz-induced superconductivity (32, 33), photoinduced metal-insulator transitions (34), ultrafast melting of charge and orbital order (35), optical and THz switching of magnetic states (36–39), and light-induced hexatic state in a layered material (40).

Now that we have identified the frequencies associated with the order parameter, we aim to trigger the phase transition by exciting the responsible vibration at its corresponding frequency. In classical simulations with point charges, vibrations can be excited by applying an oscillating electric field ($\boldsymbol{E}(t, \boldsymbol{r}) = \boldsymbol{E}(t) + \boldsymbol{r}\nabla\boldsymbol{E}(t)$) which leads to an additional force to the atoms. Dipole-allowed vibrations respond to the electric field directly whereas symmetrical vibrations can be triggered by the electric field gradient. Experimentally strong field gradients can be generated by single-cycle THz generation via optical rectification, though the achievable strength is limited by material parameters (41). In the simulations, we obviously have no such limitations.

Fig. 4 *A* and *B* show the attempts of pumping the 1.0 to 1.5 THz mode by applying an oscillating electric field and electric field gradient at 1.2 THz, respectively. The pulses are plotted in pink and blue, respectively, and the temperature of the system in red. The structural changes due to the pulse can be followed in terms of crystal axis lengths *a* (purple) and *c* (orange) and the two dihedral angles θ and ϕ (dark and light green). The electric-field pulse appears not to lead to the adsorption of energy, as indicated by the minimal temperature increase, nor to any structural changes. A clear induced phase transition can be observed, if an oscillating electric-field-gradient pulse is applied instead, coinciding with a temperature increase and sudden changes in *a*, *c*, θ, and ϕ. This indicates that the 1.0 to 1.5 THz feature is Raman and not IR active, in excellent agreement with the observation of this mode in the experimental Raman spectra and our calculated IR spectra (*SI Appendix*). The changes immediately follow the temperature increase with no additional delay, indicating that the phase transition does not require the transfer of thermal energy into other vibrational modes except for this low-frequency mode. It is important to note that these simulations were performed in the isoenthalpic–isobaric ensemble (*NPH*), meaning the system was not additionally cooled. However, it is clear from Fig. 4

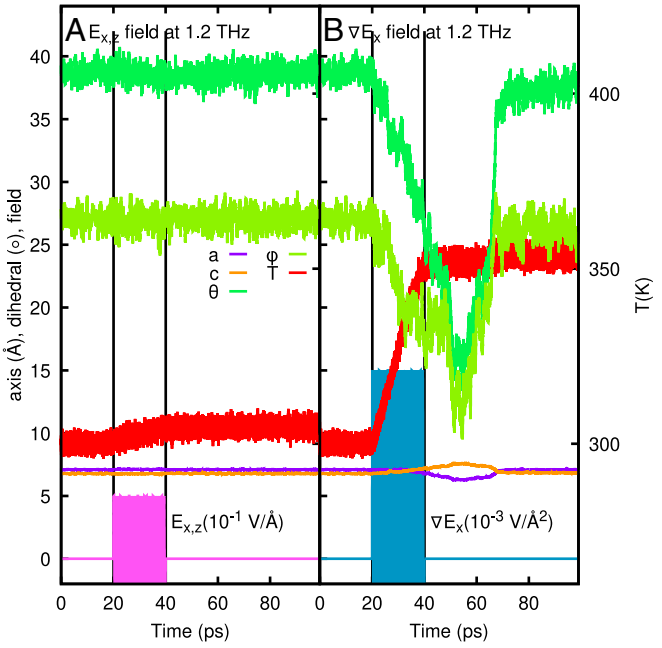

Fig. 4. Simulation of triggering the phase transition by an (*A*) oscillating electric field and (*B*) oscillating electric field gradient. (*A*) For the electric field, no energy is adsorbed and no phase change can be observed. (*B*) For the field gradient, the temperature (in red) increases and simultaneously the system transforms to β, measured by a, c, θ, and ϕ. After the pulse ends, the system relaxes back to the initial α from.

that the maximum temperature (350 K) remained well below the phase transition temperature of roughly 430 K, confirming that the phase transition was purely triggered by the induced vibrations and not by temperature. As soon as the pulse ends, the system relaxes back within 10 ps to the stable α form, still at 350 K. For the simulations in Fig. 4*B*, the electric field gradient was applied along the x axis. Gradients along y and z did not result in any transition. A movie of the trajectory is provided in *SI Appendix*. Additional simulations were performed to test the effect of the pulse duration (*SI Appendix*, Fig. S6*C*) and pulse intensity (*SI Appendix*, Fig. S6*D*) on the photoinduced phase transition. Stronger pulses lead to a longer existence of the transient metastable form, whereas weaker and shorter pulses result in a shorter transient β state. Simulations of excitation of the mode around 3.8 THz are also presented in *SI Appendix*. From these simulations, we conclude that at this frequency there are two coincidence features, one IR active and one Raman active, that are associated with changes in θ and ϕ, but not directly with the phase transition.

In conclusion, when a THz pulse with the proper intensity and resonant frequency is applied, the phase transition occurs instantaneously. The phase transition observed in Fig. 4 is induced by directly triggering the responsible low-frequency mode and is accompanied by energy absorption. There is no need for any redistribution of energy in this process. Once the pulse ends the system reverts within 10 ps back to its initial α form.

Discussion

In summary, using MD simulations, we have accurately identified the order parameter (or reaction coordinates) for the first-order phase transition between two phases of the thermosalient crystal 4DBpFO, characterized by two drastically different shapes. This order parameter includes the combined changes in dihedral angles θ and ϕ between the phenyl rings of the constituent 4DBpFO molecules. The validity of the used potential energy landscape was further confirmed by the excellent agreement between the simulated and experimentally obtained crystallographic parameters (lattice constants and dihedral angles) for the two phases. The ultrafast phase transition could be simulated without hysteresis upon heating and cooling because of the disappearance of a critical nucleus for the transition as shown by the free energy curves. This is likely because of the relatively small local molecular rearrangement required for the phase transition. These small movements are propagated by the crystal structure to result in a macroscopic mechanical change.

From the strongly fluctuating values of the dihedral angles, we generated a spectrum for the order parameter and for each individual dihedral angle during the phase transition. This allowed us to construct a THz roadmap of the transition, explicitly resolving the modes and the changes in their corresponding frequencies and widths during the phase transition. Experimental Raman spectra as a function of the order parameter, obtained by scanning the excitation laser beam across a phase boundary separating the two phases, are in excellent agreement with these simulation results. Ultimately, we tested the viability of triggering the phase transition by applying a pulse of an electric field gradient around 1.5 THz that exhibited a resonance with changes in both dihedral angles, subsequently leading to the successful nonthermal triggering of the phase transition on a picosecond timescale. The observation that the transition was triggered by a quadrupole instead of a dipole term is consistent with the Raman activity of the particular mode.

The ability to deliberately trigger a phase transition in a thermosalient crystal by exciting the contributing vibrations has significant implications for both industrial and research applications. The insights gained from the study of this THz-photoinduced mechanism open up the possibility of creating a new class of organic devices in which the mechanical, optical, magnetic, and conduction properties can be controlled and tuned on a THz time scale. The metastability of the photoinduced phase transition ensures a unique ultrafast conversion both in the forward and back transition. The almost infinite richness of relatively easily synthesizable organic molecules allows for modulation of the THz positions of the band and the transition temperature by small changes in the 3D crystal landscape and chemical structure of the organic molecules. The presented theoretical methodology can be employed to in silico investigate polymorphic forms or phase transitions of interest, and the perfect THz pulse shape to achieve specific performance.

Materials and Methods

Computational Methods. MD simulations of 4DBpFO were performed using the LAMMPS (23 June 2022) software package (42, 43). Datafiles of both the α and β structures were prepared with the use of VMD (44).

The GAFF2.1 force field was used for the intra- and intermolecular interactions (45) in combination with EEM–PESP point charges. The latter were calculated with the help of Molden (46, 47). We applied minor changes to the Lennard-Jones parameter of the hydrogen atom ($\sigma = 2.6455$ instead of 2.6255 Å) to obtain better relative stability of both forms. The final parameterization of both forms can be found in provided data files (*SI Appendix*). For all interactions, the dispersion contribution cut-off is at 10.0 Å, and the Coulombic part of the potential is computed using a particle–particle particle–mesh solver with a relative RMS error in per-atom force of 10^{-6}. The simulations are performed in the triclinic *NPT* ensemble with a time step of 0.5 fs. The thermostat and barostat parameters are set to 40 and 400 fs, respectively.

Both forms have two molecules in the unit cell, each with two θ and two ϕ angles, which gives four symmetry-equivalent angles per unit cell: two with positive and two with negative signs. Averages of these four different ϕ and θ torsional angles are obtained from all replications in the simulation cell. The resulting eight average angles are combined into a path collective variable (48, 49) that describes the $\alpha \leftrightarrow \beta$ transition. The start and end points of the paths are α and β forms respectively. The former is obtained from the simulation at 400 K and the latter at 450 K (Table 1). The path is initialized as a straight interpolation between the α and β values for the eight torsional parameters. The path was further optimized during an initial metadynamics run at 425 K. The optimized path was then employed at all temperatures.

One-dimensional metadynamics simulations were performed using the PLUMED plugin (48–51) with s as CV. A simulation cell of $8 \times 1 \times 8$ crystallographic unit cells was used which consisted of 256 molecules. The Gaussians had a width of $\sigma = 0.1$ and a step-wise reducing height: a height of 0.1 cal/mole was applied for 250 ps, followed by another two 250 ps sequences of 0.05 cal/mole and 0.025 cal/mole, and finally 0.0125 cal/mole for an additional 1 ns. A harmonic restraint of 1.5 kcal/mole on z was used to keep the system relatively close to the original path. These values are all given per mole molecules instead of per mole simulation cells, which means that the initial Gaussian height for the standard simulation cell size of $8 \times 1 \times 8$ crystallographic unit cells is 0.0256 kcal/(mole simulation cells). This standard size corresponds to a simulation cell of roughly 50 Å in all three dimensions. Control simulations were performed for different simulation cell sizes to test the robustness of the results and similar free energy curves were obtained. In these simulations, the harmonic restraints and Gaussian heights were scaled according to the system size.

The frequencies corresponding to the modes associated with the order parameter can be determined by recording s as a function of time and taking the Fourier transform of the autocorrelation function $\langle \delta s(0) \delta s(t) \rangle$. Spectra are typically obtained during constant volume simulations (*NVT*) to ensure that no volume fluctuations due to the simulation barostat appear. The exact peak positions of the resulting spectra depend on the cell dimensions during the constant volume calculations. The presented spectra in Fig. 3*A* are averages of several spectra obtained at slightly different cell dimensions. The initial configurations and volume settings for the *NVT* calculations are taken from constant pressure (*NPT*) trajectories. Here, a range of different initial structures has been taken to probe different configurations along the transition pathway. The average s during the *NVT* calculation gives an indication of the progress. We obtained 44 spectra in this way, all fluctuating around slightly different s values. These spectra were then grouped based on their mean s value and averaged per group. The resulting six spectra are shown in Fig. 3*A*.

Sample Preparation. The synthesis of the 4DBpFO compound is described in previous work (52). The α-phase crystal was grown via injection of a saturated solution in chloroform into heptane that acts as an antisolvent and forces the compound to crystallize. Well-defined parallelogram-shaped microcrystals with side lengths varying from 50 to 100 μm were formed after 2 to 3 wk. Single crystals for Raman measurements are prepared by drop-casting the freestanding microcrystals suspensions onto glass substrates. The experiments were well reproducible from crystal to crystal, though the exact phase transition temperature could vary to some degrees.

Raman characterization. The line-scan Raman spectra were recorded with a micro-Raman Horiba LabRAM HR Evolution system in the 20 to 2,500 cm^{-1} spectral range at the Department of Chemistry, University of Coimbra, Portugal. Excitation was provided by a HeNe laser ($\lambda = 633$ nm, linearly polarized) which was focused on the sample by a microscope objective ($\times 100$ magnification). The Raman signal was dispersed using an 1,800 g mm^{-1} grating resulting in a spectral resolution of ~ 2 cm^{-1}. The spectrometer calibration was performed using the characteristic crystalline Si Raman band at 521 cm^{-1} (53). The laser power at the sample was kept at around 1 mW, minimizing local heating of the sample that may cause degradation. During the line scan, a temperature-controlled heating stage THMS600 (Linkam Scientific) was used to maintain the temperature on the sample with an accuracy of ± 0.1 °C. The collection time was set to 10 s with 20 accumulations averaged to produce the final spectra.

The first-order character of the thermosalient phase transition in 4DBpFO leads to the possibility of observing the coexistence of the α phase and β phase at a fixed temperature (54). This coexistence allows a line scan experiment that provides insight into the mode changes at the transition from the α phase to the β phase without being obscured by temperature-induced effects. An in situ Raman scan was carried out across the phase boundary at a fixed temperature of 455.6 ± 0.1 K with a scanning length of 13 μm and a step size of 0.8 μm (*SI Appendix*, Fig. S8). The results were plotted as a function of s, with $s = 0$ in the α phase, $s = 1$ in the β phase and linearly extrapolating for $0 < s < 1$ in between.

Data, Materials, and Software Availability. Input scripts for the simulations are available in the supporting information and deposited at Radboud Data Repository (https://doi.org/10.34973/j5ax-am79) (55).

ACKNOWLEDGMENTS. H.M.C. and S.G. would like to acknowledge the Radboud University for financial support. Financial support from the Netherlands Organization for Scientific Research, Laserlab-Europe [European Union Horizon 2020 (EU-H2020) 871124], the China Scholarship Council, the EU-H2020, and innovation program under the European Research Council ERC Grant Agreement No. 856538 (3D-MAGiC) are gratefully acknowledged.

Author affiliations: [a]Institute for Molecules and Materials, Radboud University, Nijmegen 6525, AJ, The Netherlands; [b]Department of Chemistry, University of Coimbra, Coimbra 3004-535, Portugal; [c]Faculty of Sciences and Letters, Department of Physics, Istanbul Kultur University, Bakirköy, Istanbul 34156, Türkiye; [d]School of Materials Science and Engineering, Nankai University, Tianjin 300350, People's Republic of China; and [e]Van't Hoff Institute for Molecular Sciences, University of Amsterdam, Amsterdam 1098 XH, The Netherlands

1. D. P. Karothu *et al.*, Exceptionally high work density of a ferroelectric dynamic organic crystal around room temperature. *Nat. Commun.* **13**, 2823 (2022).
2. O. Sato, Dynamic molecular crystals with switchable physical properties. *Nat. Chem.* **8**, 644 (2016).
3. M. A. Garcia-Garibay, Molecular crystals on the move: From single-crystal-to-single-crystal photoreactions to molecular machinery. *Angew. Chem.* **46**, 8945 (2007).
4. P. Naumov, S. Chizhik, M. K. Panda, N. K. Nath, E. Boldyreva, Mechanically responsive molecular crystals. *Chem. Rev.* **115**, 12440 (2015).
5. P. Commins, I. T. Desta, D. P. Karothu, M. K. Panda, P. Naumov, Crystals on the move: Mechanical effects in dynamic solids. *Chem. Commun.* **52**, 13941 (2016).
6. C. M. Reddy, G. Rama Krishna, S. Ghosh, Mechanical properties of molecular crystals–Applications to crystal engineering. *CrystEngComm* **12**, 2296 (2010).
7. Y. Duan *et al.*, Robust thermoelastic microactuator based on an organic molecular crystal. *Nat. Commun.* **10**, 4573 (2019).
8. M. Savoini *et al.*, THz generation and detection by fluorenone based organic crystals. *ACS Photonics* **5**, 671–677 (2018).
9. S. C. Sahoo, M. K. Panda, N. K. Nath, P. Naumov, Biomimetic crystalline actuators: Structure–kinematic aspects of the self-actuation and motility of thermosalient crystals. *J. Am. Chem. Soc.* **135**, 12241 (2013).
10. C. Brandel *et al.*, Mechanisms of reversible phase transitions in molecular crystals: Case of Ciclopirox. *Chem. Mater.* **27**, 6360 (2015).
11. J. D. Dunitz, Phase transitions in molecular crystals: Looking backwards, glancing sideways. *Phys. Scr.* **91**, 112501 (2016).
12. F. H. Herbstein, On the mechanism of some first-order enantiotropic solid-state phase transitions: From Simon through Ubbelohde to Mnyukh. *Acta Cryst. B* **62**, 341 (2006).
13. M. M. H. Smets *et al.*, On the mechanism of solid-state phase transitions in molecular crystals–The role of cooperative motion in (quasi)racemic linear amino acids. *IUCrJ* **7**, 331 (2020).
14. Y. Mnyukh, *Fundamentals of Solid-State Phase Transitions, Ferromagnetism and Ferroelectricity* (DirectScientific Press, 2010).
15. S. Ghasemlou, H. M. Cuppen, Mechanism of phase transition in DL-methionine: Determining cooperative and molecule-by-molecule transformations. *ACS Omega* **9**, 3229 (2024).
16. E. Ahmed *et al.*, Ultrafast, light, soft martensitic materials. *Adv. Funct. Mater.* **32**, 2112117 (2022).
17. R. Martoňák *et al.*, Simulation of structural phase transitions by metadynamics. *Z. Kristall.* **220**, 489 (2005).
18. P. G. Karamertzanis, P. Raiteri, M. Parrinello, M. Leslie, S. L. Price, The thermal stability of lattice-energy minima of 5-fluorouracil: Metadynamics as an aid to polymorph prediction. *J. Phys. Chem. B* **112**, 4298 (2008).
19. A. Laio, M. Parrinello, Escaping free-energy minima. *Proc. Natl. Acad. Sci. U.S.A.* **99**, 12562 (2002).
20. D. Branduardi, F. L. Gervasio, M. Parrinello, From A to B in free energy space. *J. Chem. Phys.* **126**, 054103 (2007).
21. G. Bussi, D. Branduardi, "Free–energy calculations with metadynamics: Theory and practice" in *Reviews in Computational Chemistry*, A. L. Parrill, K. B. Lipkowitz, Eds. (Wiley, 2015), vol. 28, pp. 1–49.
22. K. F. Kelton, A. L. Greer, "Nucleation in condensed matter: Applications in materials and biology" in *Pergamon Materials Series*, K. F. Kelton, A. L. Greer, Eds. (Pergamon, 2010), vol. 15.
23. J. A. van den Ende, B. Ensing, H. M. Cuppen, Energy barriers and mechanisms in solid–solid polymorphic transitions exhibiting cooperative motion. *CrystEngComm* **18**, 4420 (2016).

24. H. M. Cuppen *et al.*, The rich solid-state phase behavior of L-phenylalanine: Disappearing polymorphs and high temperature forms. *Cryst. Growth Des.* **19**, 1709–1719 (2019).
25. S. Ghasemlou, B. Ensing, H. M. Cuppen, Simulation of solid-state phase transition in DL-methionine. *CrystEngComm* **25**, 3618 (2023).
26. M. D. King, P. M. Hakey, T. M. Korter, Discrimination of chiral solids: A terahertz spectroscopic investigation of L- and DL-serine. *J. Phys. Chem. A* **114**, 2945 (2010).
27. D. G. Allis, T. M. Korter, Theoretical analysis of the terahertz spectrum of the high explosive PETN. *ChemPhysChem* **7**, 2398 (2006).
28. P. M. Hakey, M. R. Hudson, D. G. Allis, W. Ouellette, T. M. Korter, Examination of phencyclidine hydrochloride via cryogenic terahertz spectroscopy, solid-state density functional theory, and X-ray diffraction. *J. Phys. Chem. A* **113**, 13013 (2009).
29. M. T. Ruggiero, W. Zhang, A. D. Bond, D. M. Mittleman, J. A. Zeitler, Uncovering the connection between low-frequency dynamics and phase transformation phenomena in molecular solids. *Phys. Rev. Lett.* **120**, 196002 (2018).
30. M. T. Ruggiero, A. J. Zeitler, T. M. Korter, Concomitant polymorphism and the martensitic-like transformation of an organic crystal. *Phys. Chem. Chem. Phys.* **19**, 28502 (2017).
31. M. Asher *et al.*, Mechanistic view on the order-disorder phase transition in amphidynamic crystals. *J. Phys. Chem. Lett.* **14**, 1570 (2023).
32. M. Mitrano *et al.*, Possible light-induced superconductivity in K3C60 at high temperature. *Nature* **530**, 461 (2016).
33. D. Fausti *et al.*, Light-induced superconductivity in a stripe-ordered cuprate. *Science* **331**, 189 (2011).
34. S. de Jong *et al.*, Speed limit of the insulator-metal transition in magnetite. *Nat. Mater.* **12**, 882 (2013).
35. P. Beaud *et al.*, A time-dependent order parameter for ultrafast photoinduced phase transitions. *Nat. Mater.* **13**, 923 (2014).
36. I. Radu *et al.*, Transient ferromagnetic-like state mediating ultrafast reversal of antiferromagnetically coupled spins. *Nature* **472**, 205 (2011).
37. S. Mangin *et al.*, Engineered materials for all-optical helicity-dependent magnetic switching. *Nat. Mater.* **13**, 286 (2014).
38. G. Li *et al.*, Ultrafast kinetics of the antiferromagnetic-ferromagnetic phase transition in FeRh. *Nat. Commun.* **13**, 2998 (2022).
39. Z. Zhang *et al.*, Terahertz-field-driven magnon upconversion in an antiferromagnet. *Nat. Phys.* **20**, 788–793 (2024).
40. T. Domröse *et al.*, Light-induced hexatic state in a layered quantum material. *Nat. Mater.* **22**, 1345 (2023).
41. B. Ferguson, X. Zhang, Materials for terahertz science and technology. *Nat. Mater.* **1**, 26 (2002).
42. S. Plimpton, Fast parallel algorithms for short-range molecular dynamics. *J. Comput. Phys.* **117**, 1 (1995).
43. A. P. Thompson *et al.*, LAMMPS–A flexible simulation tool for particle-based materials modeling at the atomic, meso, and continuum scales. *Comput. Phys. Commun.* **271**, 108171 (2022).
44. W. Humphrey, A. Dalke, K. Schulten, VMD: Visual molecular dynamics. *J. Mol. Graph.* **14**, 33 (1996).
45. D. A. Case *et al.*, Amber 2016 (2016). https://ambermd.org/doc12/Amber16.pdf. Accessed 17 October 2024.
46. G. Schaftenaar, J. Noordik, Molden: A pre- and post-processing program for molecular and electronic structures. *J. Comput. Aided Mol. Des.* **14**, 123 (2000).
47. G. Schaftenaar, E. Vlieg, G. Vriend, Molden 2.0: Quantum chemistry meets proteins. *J. Comput. Aided Mol. Des.* **31**, 789 (2017).
48. A. Pérez de Alba Ortíz, A. Tiwari, R. C. Puthenkalathil, B. Ensing, Advances in enhanced sampling along adaptive paths of collective variables. *J. Chem. Phys.* **149**, 072320 (2018).
49. G. Díaz Leines, B. Ensing, Path finding on high-dimensional free energy landscapes. *Phys. Rev. Lett.* **109**, 020601 (2012).
50. The PLUMED Consortium, Promoting transparency and reproducibility in enhanced molecular simulations. *Nat. Methods* **16**, 670 (2019).
51. G. A. Tribello, M. Bonomi, D. Branduardi, C. Camilloni, G. Bussi, PLUMED 2: New feathers for an old bird. *Comput. Phys. Commun.* **185**, 604 (2014).
52. Y. Duan *et al.*, Aggregation induced enhancement of linear and nonlinear optical emission from a hexaphenylene derivative. *Adv. Funct. Mater.* **26**, 8968 (2016).
53. B. A. Nogueira, A. Milani, C. Castiglioni, R. Fausto, The correlation between experimental polarized Raman spectra and their density functional theory prediction in the LCAO framework: The *R3c* $LiNbO_3$ crystal as a test case. *J. Raman Spect.* **52**, 995 (2021).
54. Y. Duan, S. Semin, P. Tinnemans, J. Xu, T. Rasing, Fully controllable structural phase transition in thermomechanical molecular crystals with a very small thermal hysteresis. *Small* **17**, 2006757 (2021).
55. S. Ghasemlou, D. R. Galimberti, H. M. Cuppen, Identifying and controlling the order parameter for ultrafast photoinduced phase transitions in thermosalient materials. Radboud Data Repository. https://doi.org/10.34973/j5ax-am79, Deposited 1 August 2024.